Geometry-driven Mass Transport Dynamics within Permeable 3D-Microstructures fabricated by Two-Photon Polymerization

Rana Mhanna, Ruchun Zhou, Ming Jin, Haiyan Pan, Decheng Wan, Davy-Louis Versace, Nelly Hobeika, Amine Khitous, Olivier Soppera, Patrick Lamielle, et al.

Geometry-driven Mass Transport Dynamics within Permeable 3D-Microstructures fabricated by Two-Photon Polymerization.

Rana Mhanna [1], Ruchun Zhou [2], Ming Jin* [2], Haiyan Pan [2], Decheng Wan [2], Davy-Louis Versace [3], Nelly Hobeika [1] , Amine Khitous, Olivier Soppera [1], Patrick Lamielle[1] , Jean-Pierre Malval*[1].

[1] *Institut de Science des Matériaux de Mulhouse, UMR CNRS 7361, Université de Haute Alsace, 15 rue Jean Starcky, Mulhouse, 68057, France*
[2] *Department of Polymer Materials, School of Materials Science and Engineering, Tongji University, 4800 Caoan Road, Shanghai, 201804, P.R. China*
[3] *Institut de Chimie et des Matériaux Paris-Est, UMR-CNRS 7182, Equipe Systèmes Polymères Complexes, 94320 Thiais, France*

Corresponding authors:

Prof. Ming Jin (e-mail: mingjin@tongji.edu.cn)

Prof. Jean-Pierre Malval (e-mail: jean-pierre.malval@uha.fr)

ABSTRACT.

The geometric scalability offered by two-photon stereolithography (2PS) has contributed to its rapid widespread into multiple well-established or emerging applications. Taking benefit of this flexible parameterization, we have developed an original fluorescence imaging method enable to map the real-time diffusion of quenching species moving throughout permeable three-dimensional (3D) microstructures with modular geometries (cone, pyramid, square…) fabricated by 2PS. In this strategy, we first methodically characterize the 2P polymerization performances of a Y-shaped triphenylamine photoinitiators series whose initiation efficiency perfectly echoes that measured upon one-photon excitation. More particularly, we show that the photoinitiation mechanism implies a covalent integration of the triphenylamine-based fluorophores into the photopolymer leading to the microfabrication of blue emissive 3D-objects which can be spatially 'switched-off' during the inner diffusion of copper (II) cations used as oxidative quenchers. The modulation of microstructures geometry not only regulates the global symmetry of diffusion profiles but also accounts for a topological control of the quenching propagation dynamics at local scale.

KEYWORDS: Two-Photon Polymerization, Photoinitiators, Micropatterning, Diffusion.

1. INTRODUCTION.

Two-photon polymerization (2PP) constitutes one of the most promising maskless stereolithography technologies[1-3] allowing the production of truly 3D-structures with high spatial resolution. The generated 3D-architectures can display a very high degree of structural details which are tailored specifically using a very flexible computing assisted parameterization which is now routinely proposed in commercially available two-photon 3D-printing systems[4]. From a fundamental point of view, the exceptional high writing accuracy of 2PP is achieved by tightly focusing of a *fs*-pulse laser into the photoactive materials. This simple optical configuration promotes an intrinsic spatial confinement of the photopolymerization reaction due to the synergistic combination of a low probable two-photon absorption process scaling quadratically with the excitation intensity and a polymerization threshold effect which can reduce drastically the elementary polymerized volume far below the focus optical dimension[5, 6]. With this respect, the typical resolution for near infrared 2PP fabrication is about 100 - 200 nm[2, 3] which clearly makes this technique an ideal toolbox for the production of intricate 3D-objects from nano- to microscale. In this context, a very large panel of functional materials have been successfully oriented toward 2PP stereolithography including molecularly imprinted polymers[7], metamaterials[8] , stimuli responsive materials[9], hydrogels[10-16], bactericidal agents[17], photoclickable dyes[12, 18] or magnetic nanoparticles[19]. Such cross-coupling strategies give rise to a new generation of integrated micro/nano devices whose functionalities performance can be modulated and amplified through geometrical and/or topological effects driven by the scale reduction. For instance, Lu et al.[20] have developed a 2PP method generating polymer-based 3D architectures incorporating a large amount of aligned carbon nanotubes whose orientation is both driven by the spatial confinement effect[21] and the laser scanning direction. As a result, it was demonstrated that the electrical conductivity of a linear microstructure fabricated with a parallel laser scanning direction was impressively amplified by three orders of magnitude as compared to that of a similar linear microstructure fabricated through a perpendicular direction. A very versatile strategy to introduce specific functionalities within the final two-photon patterned materials consists in implementing the added value either into the cross-linkable prepolymer or into the two-photon activable initiator. Concerning the first approach, Sun et al.[9] fabricated for instance a biomimetic microlens whose focal distance can be reversibly tuned by changing the pH value. The corresponding 2PP-compatible formulation

comprised a bovine serum albumin used as the cross-linkable stimuli responsive protein and the methylene blue as two-photon sensitizer. In the second alternative method, Versace et al.[17] have for instance developed a light-triggered antimicrobial approach based on the 2PP fabrication of 3D polyacrylate microcages with embedded curcumin dyes which led to 95 % bacteria mortality after only 10 min of visible-light exposure. In this highly virulent bactericidal strategy, the 2PP formulation simply consists in a triacrylate monomer associated with the curcumin dye playing a pivotal role as two-photon initiator and as reactive oxygen species photogenerator. In line with this latter methodology, we present herein a multifunctional two-photon initiators series whose 2PP properties and performances are first methodically investigated. We show that the free radical photoinitiation mechanism of these Y-shaped multipolar dyes (see **Scheme 1**) leads to an efficient covalent integration of the triphenylamine fluorophores into the native two-photon generated macrostructure. By cross-coupling such an unexpected blue emissive property with the permeability of the 3D-microstructure, we develop an original fluorescence mapping method to probe at local scale the real-time diffusion of an oxidative quenching reaction whose propagation dynamics can be judiciously modulated with the geometry and topology of the 3D-microstructures.

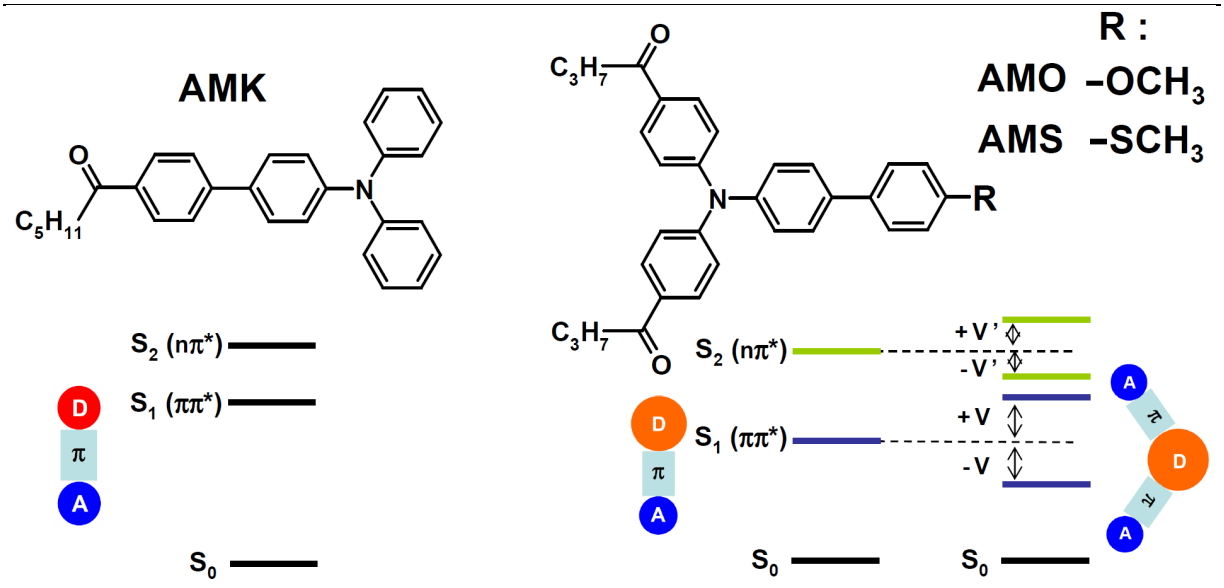

Scheme 1. Molecular structures of the chromophores and their electronic level diagrams connected to the excitonic model.

2. EXPERIMENTAL SECTION.

2.1 Materials. The synthesis and the characterization of all the triphenylamine-based chromophores are described elsewhere[22]. *N*-methyl diethanolamine (**MDEA**), copper (II) perchlorate hexahydrate, Rhodamine B, polyethylene glycol diacrylate monomer (**PEGDA**, M_n 575) and pentaerythritol triacrylate (**PETIA**) were purchased from Aldrich. All the solvents which are spectroscopic grade were also purchased from Aldrich.

2.2 Steady-state absorption and fluorescence spectra. The absorption and fluorescence spectra were recorded using a Perkin Elmer Lambda 2 spectrometer and a FluoroMax-4 spectrofluorometer.

2.3 Cyclic voltammetry and spectroelectrochemistry. The redox potentials of all triphenylamines were measured by cyclic voltammetry using a Radiometer Voltalab 6 potentiostat. All measurements were performed in N_2-saturated acetonitrile with 0.1 M of $(nBu)_4NPF_6$ used as supporting electrolyte. The cyclic voltammograms (CVs) were recorded using a three-electrode cell with a platinum disk as working electrode. A platinum wire was used as auxiliary electrode. All cell potentials were measured based on a saturated calomel electrode (SCE) reference which was placed in a separate compartment with a salt bridge containing the supporting electrolyte. The spectroelectrochemical measurements were carried out at the surface of a semi-transparent platinum gauze working electrode using a PEEK-based microcell in three-electrode configuration which is described in reference [23]. Similarly to cyclic voltammetry, the spectroelectrochemical measurements were performed in N_2-saturated ACN with 0.1 M of $(nBu)_4NPF_6$.

2.4 Two-photon excitation fluorescence. The two-photon absorption (2PA) spectra of the dyes in dichloromethane (DCM) were recorded using the two-photon excitation fluorescence (2PEF) method[24] based on femtosecond pulse laser excitation with a mode-locked Ti: Sapphire laser (Coherent, Chameleon Ultra II: pulse duration: ~140 fs; repetition rate: 80 MHz; wavelength range: 680-1040 nm). The technical details relative to the 2PEF set-up are described elsewhere[25]. All 2PA cross-sections (δ) were determined using fluorescein in water at pH = 11 as standard[26, 27]. The experimental error on the reported δ is 15 %.

2.5 Free radical one-photon polymerization. The kinetics for free radical photopolymerization was conducted *in situ* using a FT-IR Thermo-Nicolet 6700 spectrometer. A drop of each acrylate-based formulation was sandwiched between two polypropylene films

to reduce the oxygen inhibition effect. A 30 µm-thick teflon spacer was also positioned to guarantee a constant thickness of the sample which is then inserted between two BaF_2 pellets and irradiated at 365 nm using a Mercury-Xenon Lamp (LC 9588/02A from Hamamatsu) equipped with a 365 nm band pass filter (A9616-07 from Hamamatsu). The photopolymerization rate was determined based on the time-dependent decrease of the vinyl C=C stretching vibration band recorded at 1630 cm^{-1}.

2.6 Two-Photon Microfabrication. A detailed description of the 3D-stereolithography set-up and the methodology can found in reference [28]. All the microstructures were fabricated upon two-photon polymerization using the same mode-locked Ti: Sapphire oscillator as employed for 2PEF. Each microstructure was fabricated based on a systematic procedure : *i)* Deposition of the formulation drop on a 18 x 18 mm glass coverslip *ii)* Direct laser writing inside the resin *iii)* Development of 3D-structure by rinsing with ethanol to wash away the unexposed resin.

2.7 Polymerization conversion rates of two-photon fabricated microstructures. The polymerization conversion rates from two-photon patterned microstructures were evaluated by surface-enhanced Raman scattering (SERS) spectroscopy. Multiple 5 x 5 arrays of polymer squares (20 x 20 µm) were two-photon fabricated on SERS-active metal surfaces. The preparation and characterization of these substrates are detailed elsewhere[29]. These surfaces consist in gold nanoparticles deposited on glass coverslips (22 x 22 mm) by a thermal dewetting method from a sputtered gold film. The SERS signals from the polymerized microstructures were recorded using a confocal micro-Raman system (LabRam 300 from Jobin Yvon-Horiba) equipped with a BX40 optical microscope from Olympus. A 532 nm diode-pumped solid-laser (CW) was used as an excitation source. The signals were collected through a 50X, 0.50-NA objective in back-scattering optical configuration by a spectrometer equipped with a thermoelectrically cooled CCD detector. The laser power was fixed at 12.3 mW with an integration time of 20 s for each SERS measurement.

2.8. Atomic Force Microscopy (AFM). AFM images were recorded using a PicoPlus 5500 atomic force microscope used in ambient atmosphere. The characterization was obtained in resonant mode using a silicon noncontact probe (Arrow Silicon SPM Sensor).

2.9 Fluorescence image microscopy. The time-dependent fluorescence quenching reactions within the 3D-microstructures were monitored using a home-made chamber composed of two PTFE pieces which were designed in order to sandwich the 18 x 18 mm glass coverslips containing the two-photon polymerized microstructures at their upper surface (see **Scheme S1A**). The PTFE cell was magnetically assembled using a sealing gasket leading to an inner volume of ~ 150 µl. The chamber is then positioned an Olympus IX73 inverted microscope equipped with a 75 W Xe lamp housing. The microstructures immerged in ACN solution were continuously excited from the bottom of the chamber at $\lambda_{exc.}$ = 365 nm through a 40X, 0.65-NA objective using an Olympus U-FUN fluorescence mirror unit composed of a 365 nm band pass filter (BP360-370), a dichroic mirror (DM410) and long pass filter (BA420IF). The epifluorescence images were recorded with a CMOS colour camera. The procedure for fluorescence image monitoring can be described as follows: *i)* 75 µl of ACN are first introduced into the chamber leading to the swelling equilibrium of the polymer microstructures. *ii)* The fluorescence images from the incubated µm-objects are collected upon excitation at 365 nm. To minimize fluorescence bleaching effects, the excitation power is then adjusted using neutral filters placed on the excitation optical path. *iii)* Fluorescence images collection is then triggered just after the rapid injection of 75 µl of an ACN of Cu^{2+} at 8 mM into the chamber. To guarantee a reliable reproducibility of the kinetics, each measurement was repeated with three similar samples (see **Scheme S1B**).

3. RESULTS AND DISCUSSION.

Figure 1 shows the one- and two-photon absorption spectra of the chromophores in dichloromethane (DCM). The 1PA spectra of these derivatives have been extensively characterized elsewhere on the basis of excitation anisotropy measurements and TD-DFT calculations[22]. Briefly, each absorption spectrum is dominated by an intensive and structureless band in the 320-430 nm range.

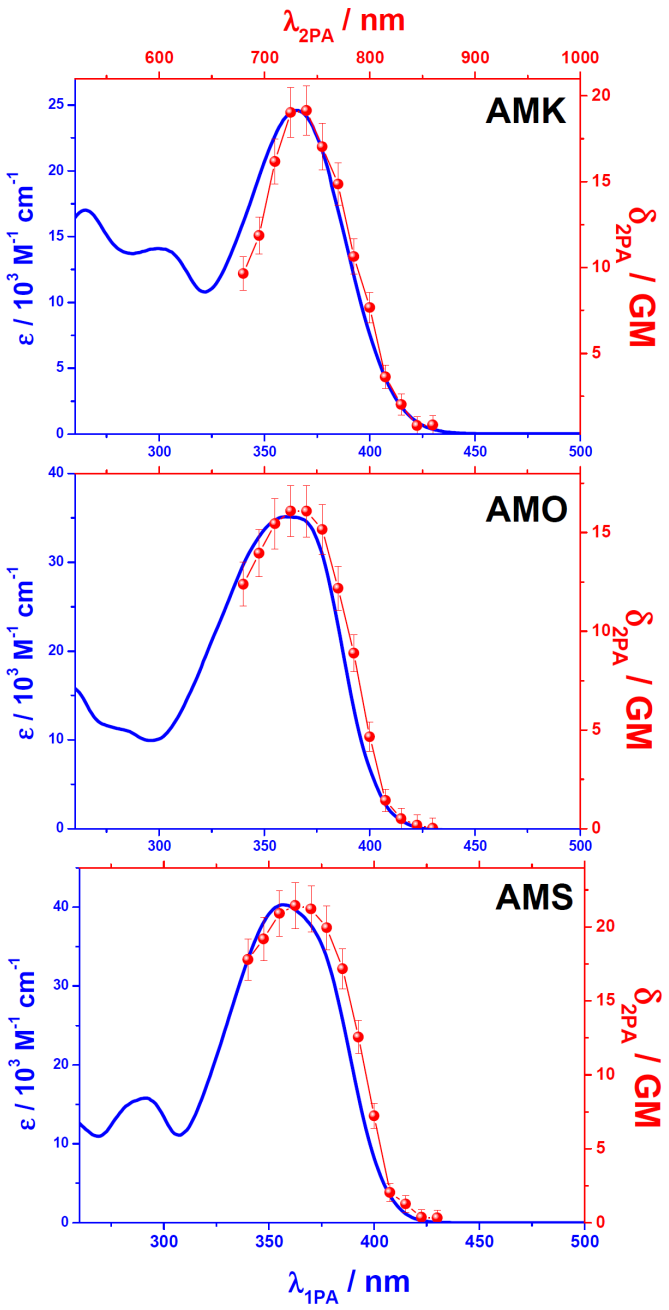

Figure 1. One- (full lines) and two-photon (circles) absorption spectra of the dyes in DCM.

For the dipolar dye **AMK**, the absorption band mainly corresponds to a ππ*-type transition (S_0-S_1 transition) implying an electronic delocalization along the D-π-A structure with a charge transfer (CT) character from the N,N'-diphenylamino group (D) to the ketone function (A). In its high energy side, the band of **AMK** also comprises a weakly allowed nπ*-type transition (S_0-S_2 transition) which is localized on the ketone function. It should be emphasized that the proximity of these two transitions leads to a S_1-S_2 vibronic coupling. This so-called 'proximity effect'[30] is responsible for the photoinitiating reactivity of **AMK** used as hydrogen abstractor reactant for free radical photopolymerization. The same structure-reactivity relationship has been derived for the Y-shaped chromophores, **AMO** and **AMS**. In this case, the absorption bands of the dyes encompass two sets of two ππ* transitions (namely S_0-S_1 and S_0-S_2 transitions) and two high-lying nπ* ones. Due to their quadrupolar symmetry (i.e. A-π-D-π-A), **AMO** and **AMS** can be seen as the juxtaposition of two equivalent dipoles whose interbranch coupling gives rise to a splitting of the initially degenerate S_n levels associated to each arm as depicted in **Scheme 1**. According to the Frenkel exciton model[31, 32], the magnitude of this interbranching coupling (V and V' in **Scheme 1**) can drastically reduce the nπ*-ππ* energy gap with a subsequent amplification of the 'proximity effect'. As shown in **Figure 1**, the 2PA band of **AMK** matches well its 1PA one. However the corresponding δ_{MAX} presents a low value of ca. 19 ± 3 GM. The weak 2PA ability of **AMK** presumably stems from the twisted geometry of its biphenyl subunit which does not guarantee an optimal π-conjugation along the dipole molecule. As a comparative example, it has been demonstrated that the value of δ_{MAX} can be enhanced by one order of magnitude[33] upon changing the biphenyl linker to a stilbenyl one. However, in the same time, the S_1-state (ππ*-type) level is strongly lowered by 0.34 eV with respect to that of **AMK**. Such a significant change in the S_1 state energy should dramatically reduce the 'proximity effect' with a detrimental impact on the photoinitiating reactivity of the dye. Therefore the choice of a biphenyl subunit as a π-electron relay constitutes a structural compromise that both guarantees two-photon activation and free radical photoinitiating ability. As displayed in **Figure 1**, the Y-shaped dyes also exhibit a weakly intensive 2PA band (δ_{MAX} ~ 16-21 GM) which globally matches their 1PA one with a very slight redshift. This 2PA band mainly corresponds to the S_0-S_1 transition of **AMO** and **AMS**. According to the dipole selection rule, the low 2PA ability observed for these quadrupolar structures[31, 34, 35] (i.e. A-π-D-π-A) is perfectly in line with the theoretically two-photon forbidden character of their lowest energy transition. Hence, despite their distinctive multipolar organisation (see **Scheme 1**), it is clearly demonstrated that all these

three dyes exhibit equivalent two-photon absorption abilities in the NIR region. However, such an equivalency does not remain true when comparing the electrochemical properties of these triphenylamine derivatives. **Figure 2A** shows the cyclic voltammograms (CVs) relative to the oxidation of the compounds in ACN.

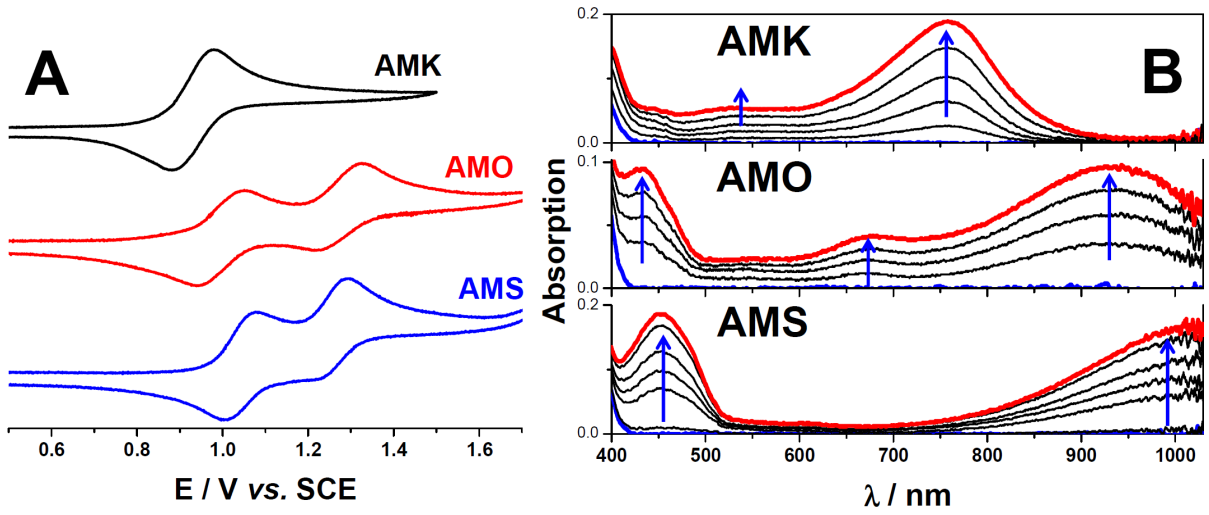

Figure 2. **A.** Cyclic voltamogramms of the compounds in ACN + $(nBu)_4NPF_6$ (0.1 M) on platinum electrode at 100 mV s^{-1} (concentration of chromophores: 10^{-3} M). **B.** Spectroelectrochemical spectra of the triphenlamine derivatives during the progressive generation of their radical cations when applying an oxidation potential at their respective E_{ox}^1 value (solvent: ACN + $(nBu)_4NPF_6$ (0.1 M)).

The CV of **AMK** presents a reversible oxidation wave (E_{ox} = 0.95 V *vs.* SCE) which leads to the generation of a N-centered radical cation whose stability contrasts to that of the triphenylamine (**TPA**$^{\bullet+}$). Indeed, it is well known that **TPA**$^{\bullet+}$ is unstable due to its rapid dimerization reaction yielding a subsequent tetraphenylbenzidine by-product[36, 37]. The rate of this oxidative radical-radical coupling can be drastically reduced by para-substitution effects on the triphenylamine group[38-40]. **AMK** typically exemplifies such a structural change with the introduction of a para π-conjugated substituent (i.e. phenone moiety). The absorption spectrum of **AMK** $^{\bullet+}$ can be easily observed by spectroelectrochemistry as presented in **Figure 2B**. The radical cation in ACN exhibits an intensive band in NIR region with a maximum at 760 nm. This band is clearly redshifted with respect to that of the tri-p-tolylamine radical cation[40] ($\Delta\lambda_{MAX}$ ~ 90 nm) which confirms the extension of the charge delocalization along the biphenyl branch. As shown in **Figure 2A**, the electrochemical behaviours of **AMO** and **AMS** are similar. Both derivatives present reversible CVs which comprise two successive one-electron oxidation waves. The first oxidation step corresponds to the formation of a stable amine-centered radical cation similarly to that observed for **AMK**

whereas the second wave leads to the generation of dication whose second positive charge is presumably located on the external anisole (**AMO**) or thioanisole (**AMS**) moiety. It is worth noting that whereas **AMO** $^{\bullet+}$ (E_{ox}^1 = 1.00 V *vs.* SCE) is generated at lower potential than **AMS** $^{\bullet+}$ (E_{ox}^1 = 1.05 V *vs.* SCE), **AMO** $^{2+}$ (E_{ox}^2 = 1.28 V *vs.* SCE) is produced at higher one than **AMS** $^{2+}$ (E_{ox}^2 = 1.23 V *vs.* SCE). This reverse electrochemical trend suggests the planarization of the **AMS** biphenyl branch which results in a higher first oxidation potential due to an extent of the π-conjugation but leads to a decrease of E_{ox}^2 consecutive to a lower coulombic repulsion between the two positive charges of **AMS** $^{2+}$ displaying a near planar quinoid-type structure[41, 42]. Interestingly, such a planarization is also in line with the bathochromic shift observed for the longest wavelength absorption band of **AMS** $^{\bullet+}$ (λ_{MAX} ~ 1020 nm) as compared to that of **AMO** $^{\bullet+}$ (λ_{MAX} ~ 930 nm). A comparable bathochromic shift can be derived when comparing the absorption spectra of the dications (see **Figure S1**). Therefore, one clearly shows that the simple change of a methoxy *p*-substituent by a thiomethyl one significantly affects the biphenyl twisted geometry upon dyes oxidation. Upon light excitation, we have previously demonstrated[22] that the deactivation of the singlet excited state of the dyes mainly proceeds through two competing relaxation processes : *i)* a radiative deactivation process from an emissive intramolecular charge transfer state (^{1}ICT) *ii)* an intersystem crossing (ISC) process generating reactive triplet species available for free radical photoinitiation. Interestingly, we showed that the ^{1}ICT state of **AMS** was highly polar with a dipole moment twice higher than that of **AMO**. This distinctive property at the excited state corroborates the consecutive electronic and geometrical changes of **AMS** during its oxidation as compared to **AMO**. Within our series, we also showed that polarity of the ^{1}ICT state indirectly regulates the ISC efficiency with a subsequent impact on the dyes photoreactivity. This original structure-reactivity relationship gives rise to a clear photoreactivity hierarchy within this triphenylamine series. More precisely we showed that **AMO** exhibits the highest reactivity when used as type II photoinitiator for free radical photopolymerization. For example, **Figure 3** shows the double bonds conversion time-profiles for different triacrylate formulations upon irradiation at 365 nm. Each bicomponent formulation comprises a viscous triacrylate monomer, the pentaerythritol triacrylate (**PETIA**, see structure in **Scheme S2**), which was mixed with the chromophores at isomolar concentration and an aliphatic amine, the N-methyl diethanol amine (**MDEA**). The first step of the photoinitiation corresponds to a hydrogen abstraction from **MDEA** to the excited triplet state of the photoinitiator which both generates a α-aminoalkyl radical (**MDEA$^\bullet$**) and the chromophore ketyl one. Due to its very

high reactivity[43], **MDEA•** is mainly responsible for a rapid addition reaction onto the double bonds of the triacrylate monomer. In **Table 1** are summarized all the photopolymerization data such as the polymerization rates (R_p/[M]) and the final conversions after 90 s irradiation.

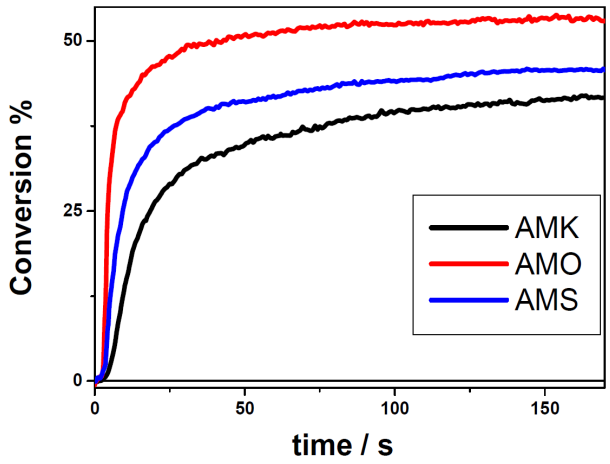

Figure 3. Real-time FTIR kinetics of C=C bonds conversion curves upon irradiation of triacrylate formulations (I_{365nm} = 15 mW cm^{-2}). Photoinitiating systems prepared at isomolar concentration of dyes (7 mM) and co-initiator **MDEA** (25 mM).

As illustrated in **Figure 3**, the conversion time-profile of **AMO** formulation presents the fastest dynamics with a C=C conversion reaching its maximum only after 90 s irradiation. By contrast, the polymerization rate (R_p/[M]) for **AMK** formulation is the lowest one among the series with a value divided by a factor ~ 3.8 and ~ 2.1 as compared to those of **AMO** and **AMS** respectively. In order to compare the intrinsic photochemical reactivity of the three photoinitiators, we have estimated the values for the relative initiation efficiency Φ_i of each formulation according the following relationship[44]:

$$\Phi_i = \frac{k_t}{k_p^2}\left(\frac{R_p}{[M]}\right)^2 \frac{1}{I_{abs}} \qquad (1)$$

In this equation, I_{abs} corresponds to the light absorbed by the sample. k_p and k_t are the rates of the polymerization propagation and termination steps respectively. These two latter parameters which mainly depend on the nature of the monomer (M) remain constant for our triacrylate formulations. The relative values for Φ_i are gathered in **Table 1**. As previously demonstrated[22], **AMO** is the highest efficient photoinitiator of the series with an initiation efficiency multiplied by a factor is 11.8 and 3.3 as compared to that of **AMK** and **AMS** respectively. Note that these amplification factors measured in highly viscous resin ($\eta_{25°C}$ ~ 1200 cps) are significantly lower than those measured previously in low viscous diacrylate formulations[22] ($\eta_{25°C}$ ~ 15 cps). Therefore, it can be derived that the medium viscosity appears

an important parameter which also drives the output of the balancing mechanism between ICT and ISC relaxation processes.

	1PA polymerization at 365 nm				2PA polymerization at 740 nm		
	I_{abs} [a] (a.u.)	R_p / [M] [b] s^{-1}	Conversion at t = 90 s (%)	Φ_i [c] (a.u.)	P_{th} / mW	δ / GM	$1/\ \delta.P_{th}^2$ / 10^{-2} GM^{-1} mW^{-2}
AMK	0.55	3.2	39	18.6	2.47	19	0.86
AMO	0.68	12.2	53	219	0.94	16	7.08
AMS	0.72	6.6	44	61	1.34	21	2.65

[a] $I_{abs} \approx I_0.\varepsilon_\lambda.[PI]$, [b] R_p / [M] : maximum of the first derivative of the conversion rate time profile, [c] Relative value which comprises the constant factor k_t/k_p^2 (see equation 1)

Table 1. One- and two-induced polymerization data relative to the triacrylate resins (Isomolar formulations of photoinitiators: 7 mM / **MDEA** : 25 mM).

This hierarchy in the photoreactivity observed for this photoinitiators series can be also extended to the two-photon polymerization. For this purpose, the two-photon initiation efficiencies of the same formulations were determined using a methodology based on the two-photon fabrication of polymer lines upon varying the laser excitation power. **Figure S2** typically shows a set of a photopatterned lines written by tightly focusing a *fs*-pulse laser beam (λ_{exc}: 780 nm) into the triacrylate formulation of **AMS** using a 40X, 0.65-NA objective. By gradually decreasing the excitation power, it is possible to determine the value of the two-photon polymerization threshold power (P_{th}) for a given excitation wavelength. This fundamental parameter corresponds to the minimum local absorbed-energy density required to promote the two-photon polymerization (see star pictogram in **Figure S2**). Interestingly, the value of P_{th} echoes the minimum concentration of radicals [R_0] which ensures the degree of monomer conversion to reach the gelation point at macromolecular scale. Therefore, [R_0] and P_{th} are connected by the following relationship[2, 45]:

$$\left[R_0\right] \propto C.\delta.\Phi_i P_{th}^2 \qquad (2)$$

Where $\delta.\Phi_i$ and C respectively correspond to the two-photon initiation efficiency and to the concentration of the photoinitiator in the formulations. It is also assumed that the initiation sequences consecutive to one- or two-photon absorption are similar in such a manner that Φ_i remains constant for both photoactivation processes. [R_0] is also considered as invariant for a given monomer. Therefore, it can be derived from equation 2 that $\delta.\Phi_i$ is proportional to $1/P_{th}^2$ for our isomolar formulations. **Figure 4A** shows the two-photon polymerization action

spectra of the formulations (i.e. $1/P_{th}^2$ *vs.* λ_{2PA}). **Table 1** gathers the corresponding two-photon polymerization data upon excitation at λ_{2PA} = 740 nm.

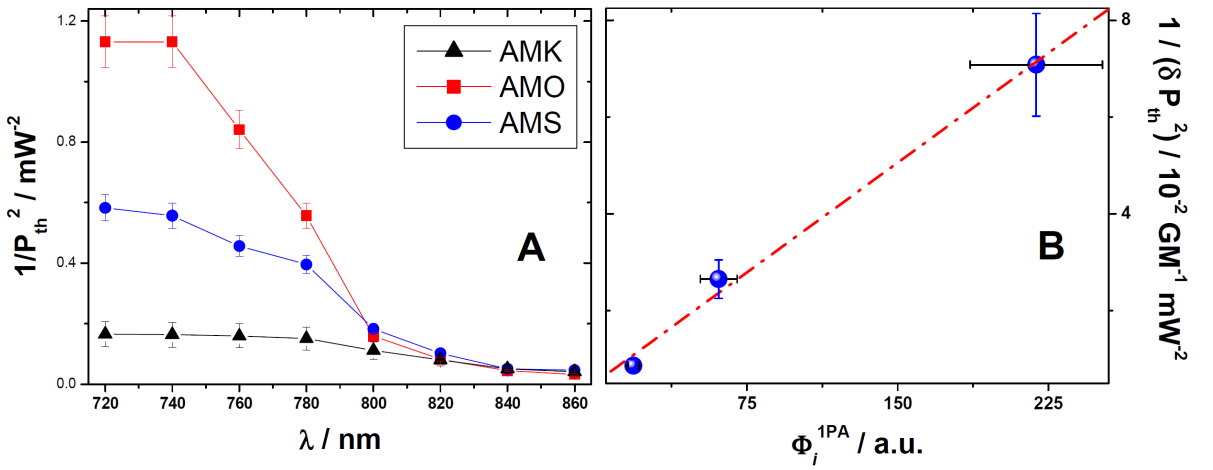

Figure 4. **A.** 2PA action polymerization spectra of the triacrylate formulations. **B.** Linear correlation between one- and two-photon polymerization efficiencies of the formulations. (λ_{1PA} = 365 nm and λ_{2PA} = 740 nm).

As shown in **Figure 4A**, each two-photon polymerization action spectrum matches very well the red edge of its corresponding 2PA spectrum (see **Figure 1**). This spectral effect clearly indicates that Φ_i is wavelength-independent upon two-photon excitation. Similarly to one-photon polymerization, **AMO** exhibits the highest initiation efficiency ($\Phi_i \sim 1/\delta.P_{th}^2$) with a relative value at 740 nm which is enhanced by a factor 8.2 and 3.1 as compared to that of **AMK** and **AMS** (see **Table 1**). Interestingly, these amplification factors agree those measured for one photon polymerization as nicely illustrated in **Figure 4B** where the initiation efficiencies of dyes upon two-photon polymerization at 740 nm ($1/\delta.P_{th}^2$) correlate very well their respective initiation efficiencies upon one-photon irradiation at 365 nm (Φ_i in **Table** 1). This correlation clearly confirms that the one- and two-photon polymerization reactions both proceed through an equivalent initiation mechanism.

From a practical point of view, we have previously shown that our triphenylamine derivatives constitute relevant type II photoinitiators for one-photon 3D-printing[22]. In the present case, we can extend their application to the domain of multiphoton 3D-stereolithography. As an illustrating example, we used **AMS** formulation with **PETIA** monomer to fabricate µm objects of arbitrary geometries. The microstructures were directly impressed into the triacrylate formulation by 3D translation of the *fs*-laser focus point. The final object is finally obtained through a development step using ethanol which dissolves

away the unexposed monomer. Due to its very efficient cross-linking ability, **PETIA** monomer leads to a very rigid macromolecular structure which guarantees the mechanical and geometrical integrity of the photopatterned structures.

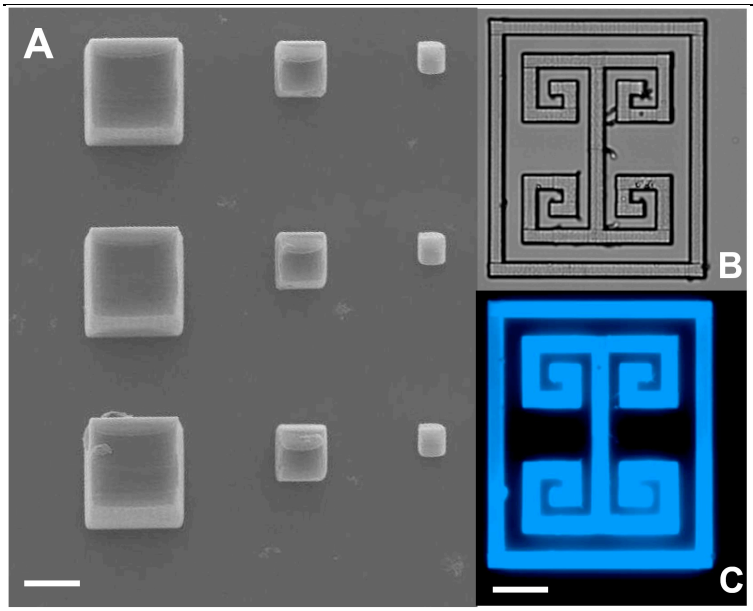

Figure 5. **A.** SEM images of representative 3D cubes structures fabricated by 2P induced polymerization. (**PETIA** with **AMS** / **MDEA** : 7 mM / 25 mM, λ_{ex} : 780 nm, P = 5 mW, τ_{exp} = 2 ms). **B-C** Transmitted light microscope image and corresponding fluorescence image of a 2D logo using the same acrylate-based formulation and the same microfabrication conditions (Scale bars: 10 µm).

For instance, **Figure 5A** shows a scanning electron micrograph (SEM) depicting an array of two-photon polymerized cubes spatially organized into a 3 x 3 matrix. On going from the left to right columns of the matrix, each cube of 15 µm side was periodically replicated applying a 1.5 homothetic size reduction factor. The SEM images of a more intricate 3D structure depicting a µm-gear with 26 cogs is also shown in **Figure S3**. Such a geometrical architecture is typically employed for MEMS applications[46, 47]. Two other microstructures are also shown in **Figure S4** and **Figure S5.** The first one presents a hollow icosahedral architecture positioned on a circular polymerized pedestal. Such a 3D microstructure which is more sophisticated than the previous one is also more fragile since its lateral edges are formed by suspended thin polymerized lines (1 µm diameter) which can be deformed due to surface tension during the final washing process. The second hollow structure in **Figure S5** exhibits an interesting waffle-like topology composed by multiple 20-µm-high vertical walls with a length of 50 µm and a very thin thickness of 450 nm which leads to a high-aspect-ratio of 44. Finally, a last example consisting in a 2D logo is depicted in **Figures 5B-C**. Interestingly, this

logo is highly fluorescent when excited at 365 nm. This blue emission presumably stems from the excitation of **AMS** by-products whose integrity of the π-conjugated triphenylamine core is preserved during the photoinitiation step. Moreover, this triphenylamine subunit should be covalently connected to polymer network due to the addition of **AMS** ketyl radical to acrylate double bonds. To demonstrate the occurrence of this parallel reaction, **Figure S6** depicts the progressive change of **AMS** fluorescence spectrum during the photopolymerization of the triacrylate formulation at 365 nm. The photopolymerization reaction induces both a total collapse of **AMS** fluorescence ICT band located at λ_{MAX} = 480 nm and the concomitant rise of a new emission band in the high energy region (λ_{MAX} = 390 nm). The significant band blueshift observed between the fluorescence spectra of **AMS** and its by-product corroborates the reduction of **AMS** ketone functions consecutive to the addition of the ketyl radical to the acrylate C=C bonds. It should be noted that an alternative radical-radical coupling process is less likely here because the resulted by-product would not be covalently linked within the polymer. To demonstrate such an effective grafting, we have prepared a new acrylate-based formulation associating the same bi-component system (i.e. **AMS** and **MDEA**) mixed with a poly(ethyleneglycol)diacrylate monomer (**PEGDA**, see **Scheme S2**). Contrary to **PETIA** resin, photopolymerization with **PEGDA** formulation leads to a permeable polymer which allows mass transport of embedded species when incubating the polymer into an imbibing solvent. According to this methodology, it is therefore possible to evaluate whether the by-products are grafted within the photopolymer or can be leached out from the macrostructure. **Figure S7** depicts the evolution of the fluorescence signal recorded from a polymerized dot during its incubation in acetonitrile (ACN). This object was fabricated by one photon polymerization at 365 nm with **PEGDA** resin and corresponds to an impressed half focus point using a 0.65-NA objective. As shown in **Figure S7**, the polymer dot radius increases by a factor ~ 1.31 in ACN which confirms the solvent uptake during the polymer swelling. In parallel, the fluorescence signal from the polymer dot as well as its fluorescence image remains perfectly invariant during 20 min incubation in ACN. Therefore, it can be derived that all the fluorophores are immobilized within the photopolymer presumably due to their covalent linkage within the matrix. Hence, the photopolymerization of **AMS** formulations leads to a photopatternable polymer that becomes emissive due to a concomitant covalent integration of the fluorophore into the native macrostructure. Such an unexpected emission property can be oriented for the real-time mapping of a well-chosen quencher diffusing within the permeable microstructure whose dimensions and geometries can be easily tuned by 3D-

stereolithograhy. As a first example, **Figure 6C** depicts the time-dependent changes of the fluorescence spatial distribution within the previous polymer dot incubated in ACN solution in presence of 4 mM of Cu^{2+}. The presence of the metal cation clearly induces a progressive fluorescence 'switch-off' of the emissive µm-object. The mechanism associated to this fluorescence quenching is well-known[37, 48, 49] and corresponds to a one-electron oxidation of the triarylamine derivatives in presence of Cu^{2+} used as chemical oxidant. In the present case, we judiciously orient this fluorescence ON-OFF redox reaction to spatially map the real-time propagation of the quenching front into the microstructure. As shown in the SEM micrograph of **Figure 6B**, the polymer dot corresponds to a truncated cone with an octagonal base of 45 µm radius. This geometry clearly leads to a radial diffusion process (see **Figure 6C**) in line with a global a cylindrical symmetry of the microstructure.

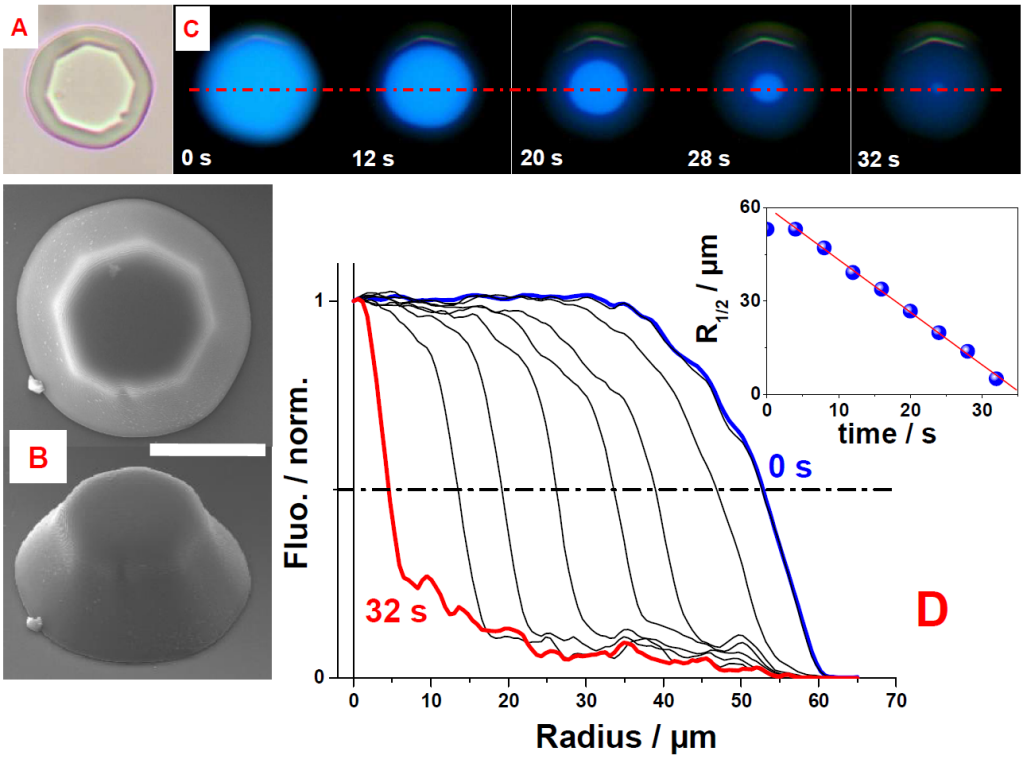

Figure 6. **A.** Optical transmitted image of the photopolymerized cone incubated in ACN. **B.** SEM images of the cone (Scale bar: 45 µm) **C.** Time-dependent fluorescence images of the polymer cone in ACN upon progressive diffusion of Cu^{2+} within the polymer network. **D.** Evolution of the fluorescence profile during the diffusion quenching process. Inset: Plot of the radius at fluorescence quenching half-time ($R_{1/2}$) as function of the diffusion time of Cu^{2+} within the polymer cone.

Figure 6D presents various normalized fluorescence profiles for distinctive diffusion times. The propagation rate of the quenching front can be derived from the time-dependent change

of the radius at half-fluorescence quenching ($R_{1/2}$) which decreases linearly with a rate of about 1.7 µm s^{-1}. Moreover the half-time fluorescence switch-off ($t_{1/2}$) of the cone is short with $t_{1/2} \sim 15$ s. Despite this very good permeability, the strong swelling of **PEGDA** gel will clearly lead to a severe loss in the spatial resolution for more intricate 3D-microsctructures fabricated by two-photon polymerization. Therefore the **PEGDA** formulation has been associated with its isomolar **PETIA** homologue to reach a reasonable compromise between polymer permeability and geometrical integrity. With this respect, we prepared a new **PEGDA** formulation comprising 0.33 molar fraction of **PETIA** cross-linking resin which leads to a two-fold reduction of the gel swelling. With this new formulation, it is also possible to demonstrate the covalent integration of **AMS** fluorophore within the polymer network during the two-photon initiation process. For instance, **Figure S8A** illustrates the invariance of the fluorescence signal recorded from a polymer square plane incubated in an ACN solution. As a comparative example, we also fabricated a similar microstructure using the same monomers but comprising **Rhodamine B** (**RhB**) as a two-photon sensitizer associated with **MDEA**. As shown in **Figure S8B**, the fluorescence of the corresponding two-photon patterned structure undergoes a significant decrease when incubated in ACN. In parallel, the surrounding solvent becomes fluorescent (see inset **Figure S8B**) which indicates a leaking of the photosensitizer residue from the incubated microstructure. Using the resin with **AMS**, **Figure 7A** shows a SEM image relative to four 20 x 20 µm square planes which were two-photon polymerized with an incremental variation of their thicknesses (L) in the 1-3 µm range.

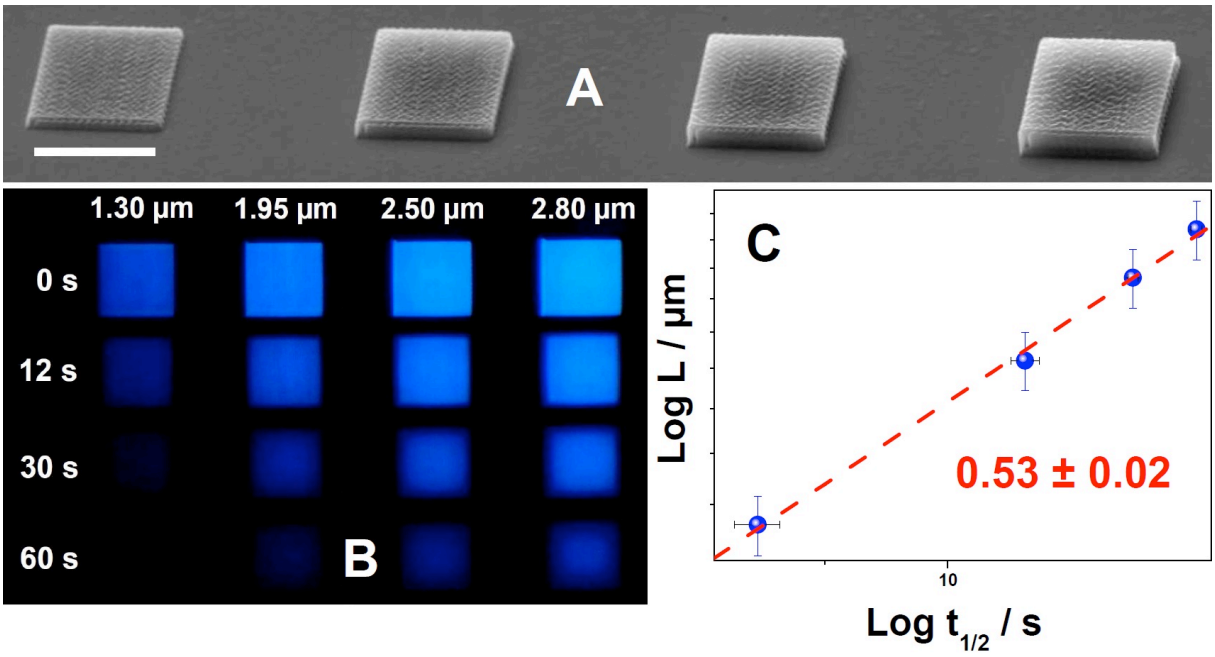

Figure 7. **A.** SEM micrographs of four polymer square planes fabricated with distinctive thicknesses. (Scale bar: 20 µm) **B.** Corresponding time-dependent fluorescence quenching images of the excited squares during their incubation in the same ACN solution with 4 mM Cu^{2+}. **C.** Log-log plots of the squares thicknesses *vs.* their corresponding quenching half-times.

Figure 7B displays fluorescence images for each square at different diffusion times. According to the symmetry of the microstructures, a *z*-diffusion process (i.e. perpendicular to the plane) is clearly privileged. For instance, the time-dependent decrease of images lateral size is ~ 3-times lower as compared to that observed along *z*-coordinate. This dominant *z*-diffusion process also follows a Fickian regime as nicely illustrated by the square-root relationship connecting planes thicknesses with their corresponding quenching half-times (see **Figure 7C**). It is worth noting that the stability and the morphology of the two-photon polymerized squares remain globally invariant after the quenching reaction. This is typically illustrated in **Figure S9** which presents the AFM images of a dried square plane whose fluorescence emission was quenched upon incubation of the structure in an ACN solution with 4 mM Cu^{2+}. Note that the shrinkage of the polymer after drying the microstructure gives rise to a surface roughness with an arithmetic average value of about 120 nm. Interestingly, the diffusivity of the quenchers within these microstructures can be modulated with the writing laser intensity. Indeed, such a photonic parameter can be adjusted in order to regulate the conversion rate of the acrylates C=C bonds and thereby the corresponding crosslink density of the two-photon patterned materials. With this respect, a set of two distinctive 20 x

20 µm square planes were fabricated on a SERS-active substrate using two different laser writing intensities (i.e. 22 µJ and 51 µJ). **Figure 8A** displays the corresponding SERS spectra along with the spectrum of the non polymerized resin which was used as a reference.

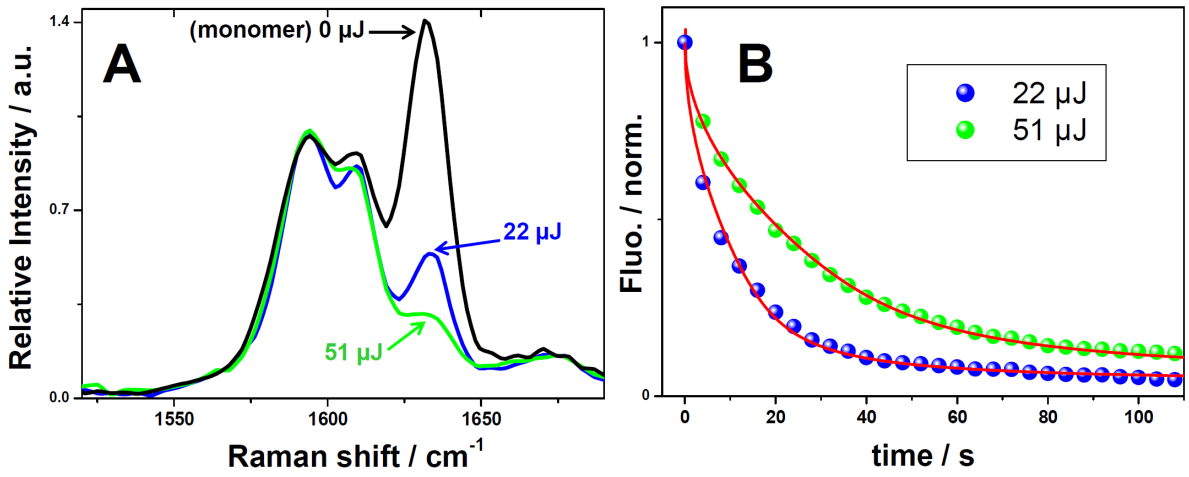

Figure 8. **A.** SERS spectra in the 1520-1690 cm^{-1} range for two 20 x 20 µm square planes which were two-photon polymerized using two distinctive laser excitation energies. All SERS spectra were normalized by the intensity of 1730 cm^{-1} ($\nu_{C=O}$ mode) **B.** Normalized fluorescence quenching kinetics of the corresponding excited squares during their incubation in an ACN solution with 4 mM Cu^{2+}. The solid lines correspond to the best-fitting curves using equation 3.

As shown in **Figure 8A**, the intensity of the SERS band located at 1631 cm^{-1} which corresponds to the stretching vibration mode of the acrylate vinyl bond decreases by a factor 1.74 when increasing the laser intensity from 22 µJ to 51 µJ. Moreover, it can be derived that the C=C bonds conversion reaches a value of 61 % for the microstructures fabricated at 22µJ whereas this conversion rate is about 78 % for structures generated at 51 µJ. Such an increase of the polymer crosslink density with the laser intensity should presumably impact the mass transport dynamics within the permeable polymer. To illustrate this effect, **Figure 8B** compares the fluorescence quenching kinetics of the corresponding square planes when incubated in an ACN solution with Cu^{2+}. Note that the thickness of each microstructure was adjusted to a similar value of L = 2.1 ± 0.2 µm. As depicted in **Figure 8B**, the fluorescence quenching dynamics within the polymer network is significantly reduced when increasing the polymer crosslink density. For instance, the quenching half-time for the polymer square plane fabricated at 51 µJ is multiplied by a factor ~ 3 as compared to its homologue fabricated at 22 µJ. In order to determine the diffusion coefficient for the quenchers, the fluorescence quenching kinetics of each microstructure were analyzed according to a planar diffusion model proposed by Winnik *et al.*[50, 51]. In this formalism which assumes that the time-dependent fluorescence quenching is mainly controlled by the progressive *z*-diffusion of the

quenchers along of the microstructure thickness, the emission intensity from the entire structures at time *t* can be expressed by:

$$I(t) = \frac{I_0}{L}\int_0^L \frac{dz}{1 + B\rho(z,t)} \qquad (3)$$

where I_0 and L denote the initial fluorescence intensity and the microstructure thickness respectively. B corresponds to a parameter connected to the response of the system at the equilibrium state ($B = I_0/I_{eq.}-1$). Since we consider that all microstructures are initially incubated in an ACN solution with a constant concentration of quenchers, the boundary condition appropriate to calculate the integral in equation (3) leads to:

$$\rho(z,t) = 1 - \frac{4}{\pi}\sum_{n=odd}^{\infty}\frac{1}{n}\exp\left(-\left(\frac{n\pi}{2L}\right)^2 Dt\right).\sin\left(\frac{n\pi}{2L}z\right) \qquad (4)$$

In equation (4), D corresponds to the global diffusion coefficient of the quencher in the photopolymer. The solid lines in **Figure 8B** show the best-fitting curves to the experimental data using least squares analysis. According to this methodology, the diffusion coefficient (D) of the quencher has a calculated value of 2.02 ± 0.04 x 10^{-2} μm^2 s^{-1} for the microstructures generated at 22 µJ whereas D is about 0.79 ± 0.05 x 10^{-2} μm^2 s^{-1} for the square planes fabricated at 51 µJ. Therefore the diffusivity of the quenchers within the two-photon patterned materials can be regulated by the laser writing intensity which indirectly drives the crosslink density of the polymer network. In the same manner, the modulation of microstructures geometry can also drive mass transport dynamics of the quenchers and consecutively the symmetry of their diffusion profiles within these permeable objects. As an illustrating example, **Figure 9** shows different time-dependent diffusion profiles within four 3D-microstructures which were two-photon polymerized with specific geometries (see insets of **Figure 9C**) : *i)* A square plane of 20 µm side and 1.5 µm thick. *ii)* A square base pyramid of 20 µm side and 20 µm height. *iii)* A similar pyramid was fabricated but with a truncation at h = 10 µm. The upper side of this truncated pyramid comprises a conical-shaped hollow with 5 µm radius and 7 µm deepness. *iv)* A 1 µm-thick polymer disk associated with two concentric annular structures of 3 µm height and with radii of 3 and 10 µm respectively. The quenching reaction progress within each microstructure has been monitored by subtracting the fluorescence image at a given diffusion time to the initial fluorescence one (i.e. $I_0(x,y) - I_t(x,y)$). According to this methodology, the real-time propagation front of diffusing quenchers can be mapped over the entire structure as depicted in **Figure 9B**.

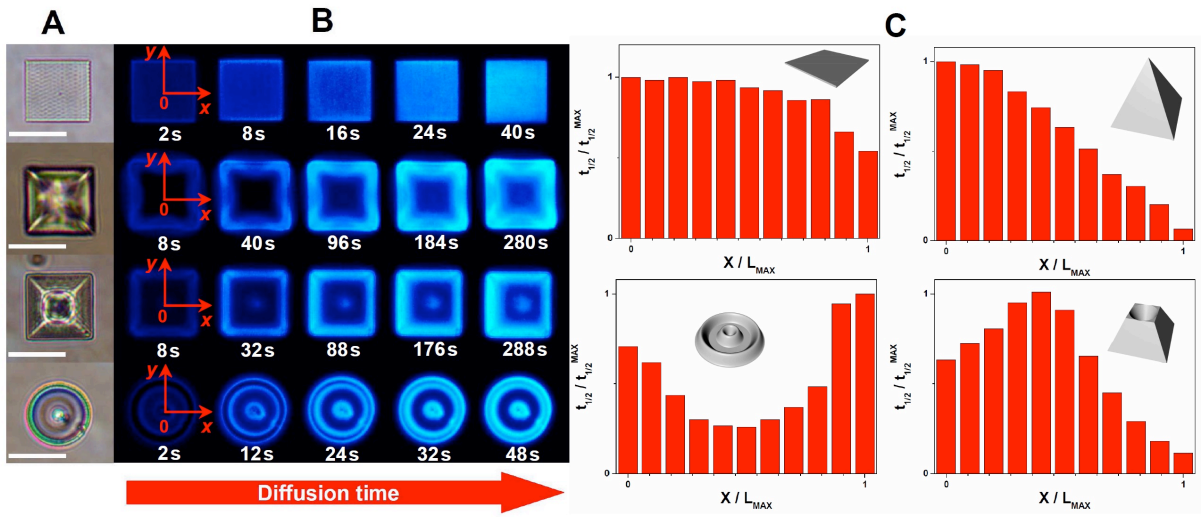

Figure 9. **A.** Optical transmitted images of various microstructures recorded in ACN solution (Scale bar: 20 µm) **B.** Differential quenching diffusion profiles within each microstructure as function of the diffusion time. **C.** Mapping of normalized quenching half-time as function of the lateral normalized *x*-coordinate for each µm-object (the *xy*-cartesian referential is shown in the image B).

Considering the propagation mode of the quenchers within the square plane, all diffusion profiles are globally independent to *xy* lateral coordinates. As shown in **Figure 9C**, such an invariance has been rationalized by plotting the *x*-dependency of the normalized quenching half-time ($t_{1/2}$ / $t_{1/2}^{MAX}$) measured by recording the fluorescence 'switch-off' kinetics at distinctive *x* coordinates from the center ($x = 0$) to the edge ($x = L_{MAX}$) of the microstructure (see **Figure S10**). As expected, this quenching half-time globally remains invariant along the *x*-coordinate which confirms an equivalent quenching dynamics irrespective to the lateral position in the square. Interestingly, the introduction of a relief within the materials clearly promotes significant changes in the symmetry of the diffusion profiles. Considering the two pyramidal structures, the quenching reaction propagates concentrically from the edge to center due to the *xy*-dependence of the materials thickness which has been purposely programmed by 3D-stereolithography. For instance, the quenching half-time for both pyramids exhibits their lowest value at $x = L_{MAX}$ in line with a very fast quenching dynamics at the thinnest zone of the structure. On going to the center of the pyramids (i.e. $x \rightarrow 0$), a significant lengthening of $t_{1/2}$ is observed as a result of the progressive increase of the thickness (see **Figure S10**). Interestingly, the presence of a deep hollow in the center of the truncated pyramid can be evidenced not only by the quenching diffusion maps (**Figure 9B**) but also by the *x*-profile of $t_{1/2}$ (**Figure 9C**). Indeed, one can observe that the quenching half-

time reaches its maximum at the middle *x*-path of the pyramid side then gradually decreases on going to the center. This is clearly in line with a reduction of the pyramid thickness when probing this hollow zone. Therefore, the evolution of $t_{1/2}$ and thereby the quenching reaction dynamics along the *x* coordinate clearly accounts for the *z*-topological of the 3D-object. With a pyramidal architecture, we showed that the quenching propagation occurs from the edge to the center with a $t_{1/2}$ maximum close to $x = 0$. As shown in **Figure 9C**, the diffusion response of two concentric annular structures with different radii results in two $t_{1/2}$ maxima for $x \approx 0$ and $\approx L_{MAX}$. As a result, the quenching dynamics alternatively accelerates and decelerates on going from the center to edge of the structure. This dynamics modulation nicely demonstrates a geometry-driven process which can be easily regulated at µm scale by 3D-multiphoton fabrication.

4. CONCLUSION.

The two-photon polymerization ability of a Y-shaped triphenylamine-based series has been methodically investigated from the dyes electronic properties to the quantification of their two-photon initiation performances. These type II photoinitiators which were initially designed for free radical one-photon polymerization in the UV-Visible range clearly display a transposable reactivity upon two-photon activation in the NIR region. More particularly, we showed that the comparative polymerization performances upon two-photon absorption parallel those measured upon one photon activation which confirms a similar initiation mechanism for both light activation processes. It is noteworthy that this mechanism implies the covalent integration of the fluorescent triphenylamine subunit into the native macromolecules giving rise to a two-photon patternable blue emissive polymer. Taking benefit of these valuable properties, we developed an original methodology using fluorescence imaging microscopy to spatially probe the real-time progress of a fluorescence quenching reaction diffusing throughout permeable 3D-microstructures whose geometry and topology are modulated by two-photon stereolithography. This strategy authorizes not only the local regulation for the reaction dynamics but also the control of the global symmetry associated to the diffusion profiles. This geometry-driven approach can be undoubtedly extended to drug delivery applications with, for instance, the 3D-fabrication of µm-reservoir whose specific geometry can presumably regulate at the local scale the dynamics of drugs release.

ASSOCIATED CONTENT.

Figure S1 : Comparison of the normalized spectroelectrochemical spectra of radical cations and dications of **AMO** and **AMS** in ACN. **Figure S2** : SEM image of 2P induced polymerized lines fabricated at distinctive laser excitation powers in order to determine the value for P_{th} of **AMS** triacrylate formulation at λ_{2PA} = 780 nm. **Figures S3-S5** : SEM images of various 2PP fabricated 3D microstrutures. **Figure S6** : Evolution of **AMS** fluorescence spectrum during the photoinitiation reaction in **PETIA** formulation upon irradiation at 365nm **Figure S7** : **A.** Transmitted optical images of a photopolymerized **PEGDA** dot in air and in ACN solution (scale bar: 40 µm). **B.** Evolution of the fluorescence signal recorded from the excited polymer dot during its incubation in ACN ($\lambda_{exc.}$ = 365 nm). **C.** Fluorescence images of the polymer dot recorded in ACN at the initial and final incubation time. **Figure S8**: Evolution of the fluorescence signals from the excitation of two-photon patterned structures with **AMS** and **RhB** (20 x 20 µm square planes) during their incubation in ACN. **Figure S9**: AFM images of a dried two-photon polymerized square plane. The fluorescence of the microstructure has been initially quenched upon incubation in an ACN solution of copper (II) cations (10^{-4} M). **Figure S10**: Time-dependent fluorescence quenching kinetics recorded at different X/L_{MAX} coordinates for each µm-structure. Insets: Initial fluorescence image with the *x*-axis referential and master 3D-image of the corresponding µm-structure. **Scheme S1** : **A.** Scheme of the PTFE chamber. **B.** Time-dependent fluorescence intensity changes relative to three similar squares planes with a thickness of 1.75 µm. **Scheme S2** : Molecular structures of the acrylate-based monomers.

CORRESPONDING AUTHORS.

* M. Jin (e-mail: mingjin@tongji.edu.cn), J.P. Malval (e-mail: jean-pierre.malval@uha.fr)

AUTHOR CONTRIBUTIONS.

Ruchun Zhou, Haiyan Pan, Decheng Wan, Min Jin : Molecular engineering, synthesis and full characterizations of the two-photon activable photoinitiators.

Rana Mhanna, Nelly Hobeika, Davy-Louis Versace: Linear and nonlinear photophysical properties of the series. In situ FTIR-photopolymerization. 3D-stereolithography.

Olivier Soppera, Amine Khitous: SEM and AFM characterizations. SERS measurements.

Patrick Lamielle: Fabrication and performances of the PTFE home-made chamber for fluorescence quenching kinetics measurements.

Jean-Pierre Malval, Ming Jin: Initiated the investigations. Draft writing, review and editing.

NOTES.

The authors declare no competing financial interest.

ACKNOWLEDGEMENTS.

This work was supported by the National Natural Science Foundation of China (51873154, 51573139).

REFERENCE.

1. C. Barner-Kowollik, M. Bastmeyer, E. Blasco, G. Delaittre, P. Müller, B. Richter and M. Wegener, *Angew. Chem. Int. ed*, 2017, **56**, 15828-15845.
2. C. N. LaFratta, J. T. Fourkas, T. Baldacchini and R. A. Farrer, *Angew. Chem. Int. ed*, 2007, **46**, 6238-6258.
3. S. Koji and C. Ya, *Appl. Phys. Rev.*, 2014, **1**, 041303.
4. S. C. Ligon, R. Liska, J. Stampfl, M. Gurr and R. Mülhaupt, *Chem. Rev.*, 2017, **117**, 10212-10290.
5. L. Li, R. R. Gattass, E. Gershgoren, H. Hwang and J. T. Fourkas, *Science*, 2009, **324**, 910-913.
6. J. Fischer and M. Wegener, *Laser Photonics Rev.*, 2012, **7**, 22-44.
7. L. P. C. Gomez, A. Spangenberg, X.-A. Ton, Y. Fuchs, F. Bokeloh, J.-P. Malval, B. Tse Sum Bui, D. Thuau, C. Ayela, K. Haupt and O. Soppera, *Adv. Mater.*, 2016, **28**, 5931-5937.
8. G. Kenanakis, A. Xomalis, A. Selimis, M. Vamvakaki, M. Farsari, M. Kafesaki, C. M. Soukoulis and E. N. Economou, *ACS Photonics*, 2015, **2**, 287-294.
9. Y.-L. Sun, W.-F. Dong, R.-Z. Yang, X. Meng, L. Zhang, Q.-D. Chen and H.-B. Sun, *Angew. Chem. Int. Ed.*, 2012, **51**, 1558-1562.
10. R. Nazir, P. Danilevicius, A. I. Ciuciu, M. Chatzinikolaidou, D. Gray, L. Flamigni, M. Farsari and D. T. Gryko, *Chem. Mater.*, 2014, **26**, 3175-3184.
11. K. Parkatzidis, M. Chatzinikolaidou, M. Kaliva, A. Bakopoulou, M. Farsari and M. Vamvakaki, *ACS Biomater. Sci. Eng.*, 2019, **5**, 6161-6170.
12. A. Ovsianikov, Z. Li, J. Torgersen, J. Stampfl and R. Liska, *Adv. Funct. Mater.*, 2012, **22**, 3429-3433.
13. J. Torgersen, X.-H. Qin, Z. Li, A. Ovsianikov, R. Liska and J. Stampfl, *Adv. Funct. Mater.*, 2013, **23**, 4542-4554.
14. A. I. Ciuciu and P. J. Cywinski, *RSC Adv.*, 2014, **4**, 45504-45516.
15. X.-C. Sun, H. Xia, X.-L. Xu, C. Lv and Y. Zhao, *Sens Actuators B Chem.*, 2020, **322**, 128620.
16. C. Lv, X.-C. Sun, H. Xia, Y.-H. Yu, G. Wang, X.-W. Cao, S.-X. Li, Y.-S. Wang, Q.-D. Chen, Y.-D. Yu and H.-B. Sun, *Sens Actuators B Chem.*, 2018, **259**, 736-744.
17. D.-L. Versace, G. Moran, M. Belqat, A. Spangenberg, R. Meallet-Renault, S. Abbad-Andaloussi, V. Brezova and J.-P. Malval, *ACS Appl. Mater. Interfaces*, 2020, **12**, 5050-5057.
18. Z. Yu, T. Y. Ohulchanskyy, P. An, P. N. Prasad and Q. Lin, *J. Am. Chem. Soc.*, 2013, **135**, 16766-16769.
19. H. Xia, J. Wang, Y. Tian, Q.-D. Chen, X.-B. Du, Y.-L. Zhang, Y. He and H.-B. Sun, *Adv. Mater.*, 2010, **22**, 3204-3207.
20. W. Xiong, Y. Liu, L. J. Jiang, Y. S. Zhou, D. W. Li, L. Jiang, J.-F. Silvain and Y. F. Lu, *Adv. Mater.*, 2016, **28**, 2002-2009.
21. S. Ushiba, S. Shoji, K. Masui, J. Kono and S. Kawata, *Adv. Mater.*, 2014, **26**, 5653-5657.
22. R. Zhou, R. Mhanna, M. Jin, H. Pan, D. Wan, D. L. Versace, C. Thomas, F. Morlet-Savary, O. Soppera and J. P. Malval, *ACS Appl. Polym. Mater.*, 2021, **3**, 3103–3113.
23. J.-P. Malval, M. Cranney, S. Achelle, H. Akdas-Kilic, J.-L. Fillaut, N. Cabon, F. R. Le-Guen, O. Soppera and Y. Molard, *Chem. Comm.*, 2019, **55**, 14331-14334
24. C. Xu and W. W. Webb, *J. Opt. Soc. Am. B*, 1996, **13**, 481-491.
25. J.-P. Malval, S. Achelle, L. Bodiou, A. Spangenberg, L. C. Gomez, O. Soppera and F. Robin-Le Guen, *J. Mater. Chem. C*, 2014, **2**, 7869-7880.
26. S. De Reguardati, J. Pahapill, A. Mikhailov, Y. Stepanenko and A. Rebane, *Opt. Express*, 2016, **24**, 9053-9066.
27. N. S. Makarov, M. Drobizhev and A. Rebane, *Opt. Express*, 2008, **16**, 4029-4047.
28. M. Jin, J. Xie, J.-P. Malval, A. Spangenberg, O. Soppera, D.-L. Versace, T. Leclerc, H. Pan, D. Wan, H. Pu, P. Baldeck, O. Poizat and S. Knopf, *J. Mater. Chem. C*, 2014, **2**, 7201-7215.
29. A. Khitous, C.-F. Lin, F. Kameche, H.-W. Zan, J.-P. Malval, D. Berling and O. Soppera, *ACS Appl. Nano Mater.*, 2021, **4**, 8770-8780.
30. E. C. Lim, *J. Phys. Chem.*, 1986, **90**, 6770-6777.
31. F. Terenziani, C. Katan, E. Badaeva, S. Tretiak and M. Blanchard-Desce, *Adv. Mater.*, 2008, **20**, 4641-4678.

32. A. S. Davidov, *Theory of molecular excitons*, Plenum Press, New York, 1971.
33. T.-C. Lin, G. S. He, P. N. Prasad and L.-S. Tan, *J. Mater. Chem.*, 2004, **14**, 982-991.
34. D. Beljonne, W. Wenseleers, E. Zojer, Z. Shuai, H. Vogel, S. J. K. Pond, J. W. Perry, S. R. Marder and J. L. Brédas, *Adv. Funct. Mater.*, 2002, **12**, 631-641.
35. M. Rumi, J. E. Ehrlich, A. A. Heikal, J. W. Perry, S. Barlow, Z. Hu, D. McCord-Maughon, T. C. Parker, H. Röckel, S. Thayumanavan, S. R. Marder, D. Beljonne and J.-L. Brédas, *J. Am. Chem. Soc.*, 2000, **122**, 9500-9510.
36. S. C. Creason, J. Wheeler and R. F. Nelson, *J. Org. Chem.*, 1972, **37**, 4440-4446.
37. K. Sreenath, C. V. Suneesh, V. K. Ratheesh Kumar and K. R. Gopidas, *J. Org. Chem.*, 2008, **73**, 3245-3251.
38. T. A. Schaub, T. Mekelburg, P. O. Dral, M. Miehlich, F. Hampel, K. Meyer and M. Kivala, *Chem. Eur. J.* , 2020, **26**, 3264-3269.
39. K. Y. Chiu, T. X. Su, J. Li, T.-H. Lin, G. S. Liou and S.-H. Cheng, *J. Electroanal. Chem.*, 2005, **575**, 95-101.
40. O. Yurchenko, D. Freytag, L. zur Borg, R. Zentel, J. Heinze and S. Ludwigs, *J. Phys. Chem. B*, 2012, **116**, 30-39.
41. N. B. Teran, G. S. He, A. Baev, Y. Shi, M. T. Swihart, P. N. Prasad, T. J. Marks and J. R. Reynolds, *J. Am. Chem. Soc.*, 2016, **138**, 6975-6984.
42. J. P. Malval, J. P. Morand, R. Lapouyade, W. Rettig, G. Jonusauskas, J. Oberlé, C. Trieflinger and J. Daub, *Photochem. Photobiol. Sci.*, 2004, **3**, 939-948.
43. S. C. Ligon, B. Husar, H. Wutzel, R. Holman and R. Liska, *Chem. Rev.*, 2014, **114**, 557-589.
44. J. P. Fouassier and J. Lalevée, *Photoinitiator for Polymer Synthesis-Scope, Reactivity and Efficiency*, Wiley-VCH Berlag GmbH & Co., Weinheim, 2012.
45. T. Baldacchini, C. N. LaFratta, R. A. Farrer, M. C. Teich, B. E. A. Saleh, M. J. Naughton and J. T. Fourkas, *J. Appl. Phys.*, 2004, **95**, 6072-6076.
46. H.-B. Sun, T. Kawakami, Y. Xu, J.-Y. Ye, S. Matuso, H. Misawa, M. Miwa and R. Kaneko, *Opt. Lett.*, 2000, **25**, 1110-1112.
47. S. Koo, *Appl. Sci.*, 2020, **10**, 8563.
48. M. Jin, J.-P. Malval, F. Morlet-Savary, H. Chaumeil, A. Defoin, P. Batat and G. Jonusauskas, *Phys Chem. Chem. Phys.*, 2009, **11**, 2622-2630.
49. C. Quinton, V. Alain-Rizzo, C. Dumas-Verdes, F. Miomandre, G. Clavier and P. Audebert, *RSC Adv.*, 2014, **4**, 34332-34342.
50. Z. Masoumi, V. Stoeva, A. Yekta, Z. Pang, I. Manners and M. A. Winnik, *Chem. Phys. Lett.*, 1996, **261**, 551-557.
51. X. Lu, I. Manners and M. A. Winnik, *Macromolecules*, 2001, **34**, 1917-1927.